A&A 677, A97 (2023)
https://doi.org/10.1051/0004-6361/202346737
© The Authors 2023

Astronomy & Astrophysics

A high-resolution radio study of the L1551 IRS 5 and L1551 NE jets*

A. Feeney-Johansson[1,2], S. J. D. Purser[3], T. P. Ray[1], C. Carrasco-González[4], A. Rodríguez-Kamenetzky[5,6], J. Eislöffel[7], J. Lim[8], R. Galván-Madrid[4], S. Lizano[4], L. F. Rodríguez[4], H. Shang[9], P. Ho[9,10], and M. Hoare[11]

[1] Dublin Institute for Advanced Studies, Astronomy & Astrophysics Section, 31 Fitzwilliam Place, Dublin D02 XF86, Ireland
[2] National Astronomical Observatory of Japan, Osawa 2-21-1, Mitaka, Tokyo 181-8588, Japan
e-mail: antonfj@astron.s.u-tokyo.ac.jp
[3] SKA Observatory, Jodrell Bank, Lower Withington, Macclesfield, Cheshire SK11 9FT, UK
[4] Instituto de Radioastronomía y Astrofísica (IRyA-UNAM), Morelia, Mexico
[5] Instituto de Astronomía Teórica y Experimental (IATE, CONICET-UNC), Laprida 854, X5000BGR Córdoba, Argentina
[6] Observatorio Astronómico de Córdoba, Universidad Nacional de Córdoba, Laprida 854, X5000BGR Córdoba, Argentina
[7] Thüringer Landessternwarte, Sternwarte 5, 07778 Tautenburg, Germany
[8] Department of Physics, The University of Hong Kong, Pokfulam Road, Hong Kong
[9] Institute of Astronomy and Astrophysics, Academia Sinica, Taipei 10617, Taiwan
[10] East Asian Observatory, 660 N. A'ohōkū Place, Hilo, HI 96720, USA
[11] School of Physics and Astronomy, University of Leeds, Leeds, UK

Received 25 April 2023 / Accepted 19 July 2023

ABSTRACT

Using observations with e-MERLIN and the *Karl G. Jansky* Very Large Array (VLA), together with archival data from the Atacama Large Millimeter/submillimeter Array (ALMA), we obtain high-resolution radio images of two binary YSOs: L1551 IRS 5 and L1551 NE, covering a wide range of frequencies from 5 to 336 GHz, and resolving emission from the radio jet on scales of only ∼15 au. By comparing these observations to those from a previous epoch, it is shown that there is a high degree of variability in the free-free emission from the jets of these sources. In particular, the northern component of L1551 IRS 5 shows a remarkable decline in flux density of a factor of ∼5, suggesting that the free-free emission of this source has almost disappeared. By fitting the spectra of the sources, the ionised mass-loss rates of the jets were derived and it was shown that there is significant variability of up to a factor of ∼6 on timescales of ∼20 years. Using radiative transfer modelling, we also obtained a model image for the jet of the southern component of L1551 IRS 5 to help study the inner region of the ionised high-density jet. The findings favour the X-wind model launched from a very small innermost region.

Key words. stars: formation – stars: low-mass – stars: winds, outflows – radio continuum: stars – radiation mechanisms: thermal

1. Introduction

Jets and outflows are observed towards young stellar objects (YSOs) ranging in mass from proto-brown dwarfs to O-type protostars, and play an important role in star formation (Frank et al. 2014). They are closely linked to accretion and help extract angular momentum from infalling matter thus permitting accretion onto the protostar (Bacciotti et al. 2002).

Observations at radio wavelengths permit studies of protostellar outflows close to their driving sources, where observations at optical and near-infrared (IR) wavelengths are difficult due to obscuration by dust. Free-free (bremsstrahlung) emission at centimetre wavelengths is commonly observed towards the base of the jet and is thought to trace material that has been ionised by internal shocks in the jet (Curiel et al. 1987). Radio observations at centimetre wavelengths can therefore help to trace material that has recently been ejected by the YSO and calculate properties such as the direction, collimation, or mass-loss rate of this recently ejected material. This can be compared with observations that track the larger-scale outflow, such as molecular outflows or optical/IR jets.

In spite of many observational studies of protostellar outflows, the mechanism by which they are launched and collimated is still broadly debated (Ray & Ferreira 2021). It is thought that material is accelerated by magnetocentrifugal forces along the magnetic field lines of either the star or disk. The two main theories are known as the X-wind model (Shu et al. 1994) and the disk wind model (Blandford & Payne 1982; Pudritz & Norman 1983). In the X-wind model, material is thought to be launched from the innermost region of the disk along the pinched stellar magnetic field lines. In the disk wind model, material is launched from the surface of the disk at a wide range of distances from the star up to tens of astronomical units along open magnetic field lines threading the disk. In both models, the material is then 'self-collimated' far beyond the Alfvén radius through magnetic hoop stresses at a large scale.

In order to learn more about the launching and collimation of jets, high-resolution observations near the base of the jet are necessary. Optical or IR emission from this region is often obscured by high levels of extinction, particularly in more embedded sources. Therefore, radio observations of the free-free emission are ideally suited for this purpose. Previous

* FITS images are only available at the CDS via anonymous ftp to cdsarc.cds.unistra.fr (130.79.128.5) or via https://cdsarc.cds.unistra.fr/viz-bin/cat/J/A+A/677/A97

Open Access article, published by EDP Sciences, under the terms of the Creative Commons Attribution License (https://creativecommons.org/licenses/by/4.0), which permits unrestricted use, distribution, and reproduction in any medium, provided the original work is properly cited.
This article is published in open access under the Subscribe to Open model. Subscribe to A&A to support open access publication.

observations at centimetre wavelengths indicate that jets are collimated on scales of only a few tens of astronomical units or less (Anglada et al. 2018). The highest-resolution observations of a low-mass protostar to date (Carrasco-González et al. 2019), suggest that in HL Tau the jet is already collimated at only ∼1.5 au from the star. On the other hand, in the high-mass YSO Cep A HW2, Carrasco-González et al. (2021) found that the jet was collimated further away from the protostar than in the case of low-mass YSOs, at ∼20−30 au. They propose two possible launching mechanisms to explain this, either a scaled-up version of the disk wind model, where the collimation distance scales with the mass of the star, or a wide-angle wind launched from the disk which is then externally collimated at large distances from the star by a large-scale magnetic field or dense ambient medium. In the intermediate-mass YSO Serpens SMM1, Rodríguez-Kamenetzky et al. (2022) suggest that its outflow consists of two components, a highly collimated narrow jet launched by the X-wind mechanism and a wide-angle wind that is launched by either the X-wind or disk wind mechanism.

In this work, we report on new high-resolution observations of two YSO systems in the L1551 star-forming region: L1551 IRS 5 and L1551 NE. L1551 is a low-mass star-forming region located in the south of the Taurus molecular cloud (TMC) at a distance of 147 ± 5 pc (Connelley & Reipurth 2018). The nearby location of this region makes it an ideal target for high-resolution observations as it allows us to resolve the regions close to the star. These observations were carried out using e-MERLIN and the *Karl G. Jansky* Very Large Array (VLA) at a range of frequencies from 5 to 26 GHz. The resolution of these observations allows us to discern emission on scales of only ∼15 au.

L1551 IRS 5 is a well-known Class I source that has been classified as a FUor object based on spectral analysis (Connelley & Reipurth 2018). These are objects that show strong outbursts in which their brightness increases by several orders of magnitude, and they are thought to be caused by rapid increases in the accretion rate of the star. Such outbursts can then last for decades (Audard et al. 2014). L1551 IRS 5 is a binary with a projected separation of ∼0.36″ or ∼50 au between the northern (N) and southern (S) components. The total mass of the system is estimated to be ∼0.5−1.0 $M_\odot$ with a mass ratio between the two components of $q \sim 1$ (Rodríguez et al. 2003a; Lim & Takakuwa 2006; Chou et al. 2014). Each has a circumstellar disk as well as a circumbinary disk surrounding the whole system (Cruz-Sáenz de Miera et al. 2019; Takakuwa et al. 2020). Both components have high mass accretion rates of $\dot{M}_{\rm acc} = 6 \times 10^{-6}\,M_\odot\,{\rm yr}^{-1}$ and $\dot{M}_{\rm acc} = 2 \times 10^{-6}\,M_\odot\,{\rm yr}^{-1}$ for the N and S components, respectively (Liseau et al. 2005). Both of the components are known to drive jets that are seen in the form of thermal ionised jet emission in the radio (Rodríguez et al. 2003b) as well as in the optical (Mundt & Fried 1983), and they are collimated within ≤3 au from the central star (Lim & Takakuwa 2006). The N jet has a position angle of 67 ± 3° while the S jet has a position angle of 55 ± 1° with the red-shifted portions of both jets pointing to the north-east and the blue-shifted portions to the south-west (Rodríguez et al. 2003b). L1551 IRS 5 was also the first source towards which a molecular outflow was detected (Snell et al. 1980). The projection angle for both circumstellar disks was estimated by Lim et al. (2016b) to be ∼45° based on VLA millimetre observations of the dust emission. From this, we can assume that the inclination angle for both jets to the line of sight is also approximately $i \approx 45°$. Based on [O I]$_{63}$ observations of the atomic jet and by comparison with other atomic and molecular emission lines, Sperling et al. (2021) determined that the atomic jet is the dominant component of the outflow and estimated the mass-loss rate of the outflow to be $\dot{M} = (4.9{-}5.4 \pm 0.8) \times 10^{-7}\,M_\odot\,{\rm yr}^{-1}$.

L1551 NE is another Class I binary system located ∼2.5′, or ∼22 000 au, north-east of L1551 IRS 5. It is comprised of a south-eastern source (known as component A) and a north-western source (known as component B) with an estimated projected separation between the two components of ∼0.5″ or ∼70 au. The deprojected separation between the two components was calculated to be ∼145 au (Takakuwa et al. 2014). The total mass of the system is estimated to be ∼0.8 $M_\odot$ with a mass ratio of $M_{\rm B}/M_{\rm A} \sim 0.19$, where $M_{\rm A}$ and $M_{\rm B}$ are the mass of component A and B, respectively (Takakuwa et al. 2012). Similar to L1551 IRS 5, each component has a circumstellar disk as well as a circumbinary disk surrounding the whole system (Takakuwa et al. 2014, 2017). Thermal ionised jet emission is also seen from both components with position angles for the jets of 48 ± 10° and 58 ± 8° for components A and B, respectively, with the red-shifted portions of both jets pointing to the north-east and the blue-shifted portions to the south-west (Reipurth et al. 2002). The outflow from L1551 NE is thought to be responsible for the HH objects HH 28 and HH 29 and a series of HH knots known as HH 454 which surrounds L1551 NE. Lim et al. (2016a) calculated the projection angles of both disks, and hence the inclination angles of both jets to the line of sight, to be ∼58° based on VLA millimetre observations. From this, the inclination angle of the jet to the line of sight is estimated to also be $i \approx 58°$.

The structure of this paper is as follows. In Sect. 2, we describe the radio observations carried out using e-MERLIN, the VLA, and the Atacama Large Millimeter/submillimeter Array (ALMA) and the data reduction process. In Sect. 3, we present the resulting images obtained and the flux densities measured at the different frequencies. In Sect. 4, we then model the spectra of the sources. This was then used to estimate the ionised mass-loss rate for each jet. The variability seen in the jets compared to previous observations is also discussed. Radiative transfer modelling is also performed for one of the jets in L1551 IRS 5. Finally, in Sect. 5, we present our concluding remarks.

2. Observations and data reduction

L1551 IRS 5 was observed using e-MERLIN, including the Lovell Mk I 76 m telescope, on 2020 January 25 in *C* Band at 5 GHz/6 cm with a total bandwidth of 0.5 GHz (Project code: LE1007). The total time-on-source was ≈16 h. Using the VLA in the A configuration, the most extended configuration for the array, L1551 IRS 5 and L1551 NE were observed at *C* Band (6 GHz/5 cm), *X* Band (10 GHz/3 cm), *Ku* Band (15 GHz/2 cm), and *K* Band (22 GHz/1.4 cm) on 2021 January 18, 15, 19, and 2020 December 29, respectively (Project code: 20B-122). All of the observations were calibrated and imaged using the Common Astronomy Software Applications (CASA; CASA Team 2022) software package (version 6.1.2). For the e-MERLIN observation, 3C286 was used as the flux calibrator, J1407+2827 was used as the bandpass calibrator, and J0428+1732 was used as the complex gain calibrator. For the VLA observations, 3C147 was used as the flux calibrator at all frequencies and was also used as the bandpass calibrator for the *C* Band and *X* Band observations. For the VLA *Ku* Band and *K* Band observations, 3C84 was used as the band pass calibrator. The source J0431+2037 was used as the complex gain calibrator in all VLA observations for both L1551 IRS 5 and L1551 NE. Self-calibration was also successfully performed for the VLA *Ku* band and *K* band observations, although it was not possible for the e-MERLIN observation nor

Table 1. Summary of observations of L1551 IRS 5.

Instrument	Date	Time	λ (mm)	ν (GHz)	$\Delta\nu$ (GHz)	TOS (min)
e-MERLIN	2020-Jan.-25	15:32:05	60	5	0.5	990
VLA	2021-Jan.-18	06:34:54	50	6	4	6
VLA	2021-Jan.-15	06:07:40	30	10	4	6
VLA	2021-Jan.-09	00:38:00	20	15	6	80
VLA	2020-Dec.-29	02:41:00	14	22	8	80
ALMA	2017-Nov.-20	04:05:30	3.2	93	8	4
ALMA	2017-Nov.-04	07:34:18	2.0	153	8	6
ALMA	2017-Jul.-24	12:23:52	1.3	225	4	11
ALMA	2017-Jul.-27	11:32:46	0.9	336	6	36

Table 2. Summary of observations of L1551 NE.

Instrument	Date	Time	λ (mm)	ν (GHz)	$\Delta\nu$ (GHz)	TOS (min)
VLA	2021-Jan.-18	06:34:54	50	6	4	6
VLA	2021-Jan.-15	06:07:40	30	10	4	6
VLA	2021-Jan.-09	00:38:00	20	15	6	80
VLA	2020-Dec.-29	02:41:00	14	22	8	80
ALMA	2019-Oct.-07	06:47:31	0.9	336	6	18

the VLA *C* band and *X* band observations due to insufficient signal-to-noise.

As well as these observations we also used archival data for our sources from ALMA. L1551 IRS 5 was observed in Band 3 (93 GHz/3.2 mm) and Band 4 (153 GHz/2 mm) on 2017 November 20 and 2017 November 4 (Project code: 2017.1.00388.S; PI: H. I. Liu), in Band 6 (225 GHz/1 mm) on 2017 July 24 (Project code: 2016.1.00209.S; PI: M. Takami), and in Band 7 (336 GHz/0.9 mm) on 2017 July 27 (Project code: 2016.1.00138.S; PI: S. Takakuwa). L1551 NE was observed in Band 7 on 2019 October 7 (Project code: 2019.1.00847.S; PI: P. Sheehan). The Band 6 and Band 7 data for L1551 IRS 5 were previously published in Cruz-Sáenz de Miera et al. (2019) and Takakuwa et al. (2020) respectively. The archival ALMA images were inspected, along with the corresponding calibration inspections plots from the archive, to ensure that the data were of a sufficiently high quality to use for our study. Details of all of the observations used in this study are given in Tables 1 and 2.

In order to achieve good *uv*-coverage and create a high-resolution image of L1551 IRS 5 at *C* Band, the visibility data from the e-MERLIN *C* band observation and the VLA *C* band observation were combined. This took advantage of the high resolution of e-MERLIN and the sensitivity and short baseline coverage of the VLA. As the observations were taken approximately a year apart, the proper motion of L1551 IRS 5 had to be accounted for, as well as any phase errors between the two observations. The two observations used different phase calibrators, and so there may have been differences in the positions of sources as a result. The absolute proper motion of the system was calculated by Villa et al. (2017) based on VLA observations at 7 mm and found to be of the order of $\mu \sim 25$ mas yr^{-1} ($\mu_\alpha = +17.4 \pm 4.0$ mas yr^{-1}, $\mu_\delta = -18.2 \pm 0.6$ mas yr^{-1}). To account for any differences in position due to phase errors, the position of the point-like field source XEST 22–054, located at the co-ordinates (J2000) RA: 04:31:43.00 and Dec: +18:10:34.5, was compared between the two images. The source was assumed to be an extragalactic source based on its steep negative spectral index ($\alpha = -2.02 \pm 0.06$) in the VLA *C* Band image and the lack of any IR detections at this position when checked using SIMBAD. Therefore it should have no significant proper motion. The difference in the RA and Dec was found to be $\Delta_\alpha = +20$ mas and $\Delta_\delta = -70$ mas respectively. When combining the proper motion and the difference due to phase errors, this gave a total difference in position between the two observations of $\Delta_\alpha = +37.1$ mas and $\Delta_\delta = -87.8$ mas. Therefore, the e-MERLIN data were shifted so that the position of L1551 IRS 5 would match the position in the VLA data using the CASA task *fixvis*. We note that there would also be proper motion of the emission knots in the jet relative to the star and disk, which cannot be corrected for since the knots in the red-shifted and blue-shifted portions would be moving in opposite directions. There is also relative proper motion of the two components with respect to each other due to orbital motion which also could not be corrected for, with the change in RA and Dec of the S component with respect to the N component being $\Delta_\alpha = -3.2 \pm 0.9$ mas yr^{-1} and $\Delta_\delta = -2.6 \pm 0.7$ mas yr^{-1} (Lim & Takakuwa 2006; Lim et al. 2016b). Since the e-MERLIN and VLA observations have different bandwidths, only the part of the VLA bandwidth corresponding to the e-MERLIN bandwidth was used so that they would have the same central frequency and bandwidth when combined into one set of data.

For all of the VLA and VLA+e-MERLIN bands, a Briggs weighting of +0.5 was used for imaging as this seemed to give the best compromise between angular resolution and sensitivity. Also, when imaging the combined e-MERLIN and VLA image, an outer *uv*-cutoff of 1.375×10^6 λ was used to show the extended emission more clearly. We note that the *Ku* Band and *K* Band data were each split into two sub-bands given their large fractional bandwidths in order to increase spectral sampling in the SED.

The total flux densities of the sources at each frequency were measured in CASA by drawing a region around each source

containing all of the emission above a certain threshold and integrating the flux within that region. The thresholds used were $3\sigma_{\rm rms}$ for the VLA and e-MERLIN images, $10\sigma_{\rm rms}$ for the ALMA Band 3 and Band 4 images, and $25\sigma_{\rm rms}$ for the ALMA Band 6 and Band 7 images. Higher thresholds were used for the ALMA images to avoid including dust emission from the circumbinary rings around the sources. For some of the images, particularly in the *C* Band image of L1551 IRS 5, there is overlap between the emission of the two sources. In these cases, the polygon was drawn so that it passes through the saddle-point of the brightness distribution between the two sources. Although this means that there is a significant degree of uncertainty in the flux density of the N component of L1551 IRS 5 at 5 GHz, due to the low level of its flux density and the high degree of overlap with the emission of the S component.

When measuring the total flux densities of the sources in the e-MERLIN and VLA observations, the data at each frequency were re-imaged, using the same outer uv-cutoff and synthesised beam for each band. This was in order to measure and compare the total flux densities at different frequencies more accurately and avoid any issues with differences in uv-coverage and synthesised beam size between the images. The uv-cutoff and synthesised beam used was the maximum baseline and the synthesised beam of the lowest resolution observation. For L1551 IRS 5, this was the *X* Band VLA observation, which gives a *uv*-cutoff of $1.375 \times 10^6\ \lambda$ and a beam of $0\farcs20 \times 0\farcs18$ with a PA of 49°. For L1551 NE, this was the *C* Band VLA observation, which gives a uv cut-off of $1 \times 10^6\ \lambda$ and a beam of $0\farcs37 \times 0\farcs30$ with a PA of 61°. We note however, that the images presented in Figs. 1–4, are the original images before all of the frequency bands were re-imaged with the same synthesised beam and *uv*-cutoff. Also we note that the synthesised beam values given in Tables 3 and 4 are the synthesised beams in the original images.

3. Results

3.1. L1551 IRS 5

L1551 IRS 5 was imaged and successfully detected in all bands. The flux densities measured for the N and S components at each frequency are listed in Table 3. The images from the VLA observations are shown in Fig. 1 in colour scale, with contours overlaid. The black crosses indicate the peaks of the disk emission from the ALMA Band 4 image (153 GHz/2.0 mm) to show the approximate positions of the central stars. The peaks in the ALMA Band 4 image were used as this was the highest-resolution image obtained. These positions have been shifted, relative to the ALMA image, to account for the proper motion between the ALMA observation and the VLA observations based on the proper motion measurements from Villa et al. (2017). The dashed white lines indicate the position angles of the jets from Rodríguez et al. (2003b).

The combined e-MERLIN and VLA *C* Band (5 GHz/6 cm) image is shown in Fig. 1a. At this frequency, it is expected that there should be very little dust emission from the disk and thermal free-free emission from the jet should be dominant. This is consistent with what is seen in the S component, where the emission is clearly elongated along the jet axis. Two main emission lobes are seen either side of the central star, with the north-east lobe corresponding to the red-shifted jet and the south-west lobe corresponding to the blue-shifted jet. In the N component on the other hand, the emission detected appears to be very weak and close to the position of the central star with no extended emission seen along the jet axis.

At the higher frequencies observed with the VLA (10−24 GHz), the emission of both sources peaks at the positions of the central stars, with extended emission seen along the direction of the jet axes of both sources. The double lobe structure seen at 5 GHz in the S component is not seen at higher frequencies. This is likely due to lower angular resolution along the jet axis as well as decreasing optical depth in the jet at higher frequencies causing the peaks of the free-free emission to be closer to the origin of the jet.

At ALMA frequencies (93−336 GHz), the emission is expected to be completely dominated by dust emission, with little or no free-free emission present. The ALMA images shown in Fig. 2 agree with this, as the emission is centred at the positions of the stars at all frequencies, with no emission seen along the jet axes.

3.2. L1551 NE

L1551 NE was successfully imaged and detected in all of the bands in which it was observed. The flux densities were measured for component A and component B at each frequency are shown in Table 4.

The images from the VLA and ALMA observations are shown in Figs. 3 and 4 in colour scale, with contours overlaid. To show the approximate positions of the central stars, the peaks of the emission from the VLA 24 GHz image are indicated by the black crosses. The peaks of the 24 GHz image were used as this was the highest-resolution image obtained. Unlike in the case of L1551 IRS 5, the peak in the dust emission seen in the ALMA 336 GHz image was not used as there was proper motion between the epochs of the ALMA observation (Oct. 2019) and the VLA observations (Dec. 2019–Jan. 2020), which was not corrected for, as no proper motion measurements were available for L1551 NE. This can be seen in the displacement between the peaks of the ALMA Band 7 image and the 24 GHz image in Fig. 4.

The dashed white lines indicate the position angles of the jets from Reipurth et al. (2002). Similar to L1551 IRS 5, we should expect to see mainly free-free emission at lower frequencies, while at higher frequencies dust emission from the disk should become dominant.

4. Discussion

4.1. Spectrum

To learn more about the emission observed from these sources, the total flux densities of the components of L1551 IRS 5 and L1551 NE were plotted as a function of frequency to give a spectrum for each source. The resulting spectra for the N and S components of L1551 IRS 5 are shown in Fig. 5. For comparison, the flux density values given by Rodríguez et al. (1998) and Rodríguez et al. (2003b) are shown in the figures as well. Both components were fitted with a model spectrum consisting of a combination of a thermal free-free emission component and a dust emission component. When modelling the free-free emission, the model from Reynolds (1986) was used. This assumes that the ionised flow in the jet begins at an injection radius above the disk along the jet axis of r_0, with an initial velocity v_0, electron temperature T_0, half-width w_0, and electron density n_0. The half-width and electron density of the jet vary with distance along the jet as $w(r) = w_0(r/r_0)^{\epsilon}$ and $n_{\rm e}(r) = n_0(r/r_0)^{q_n}$ respectively. A conical jet model was used for which $\epsilon = 1$, $q_n = -2\epsilon = -2$ and the electron temperature and velocity of the

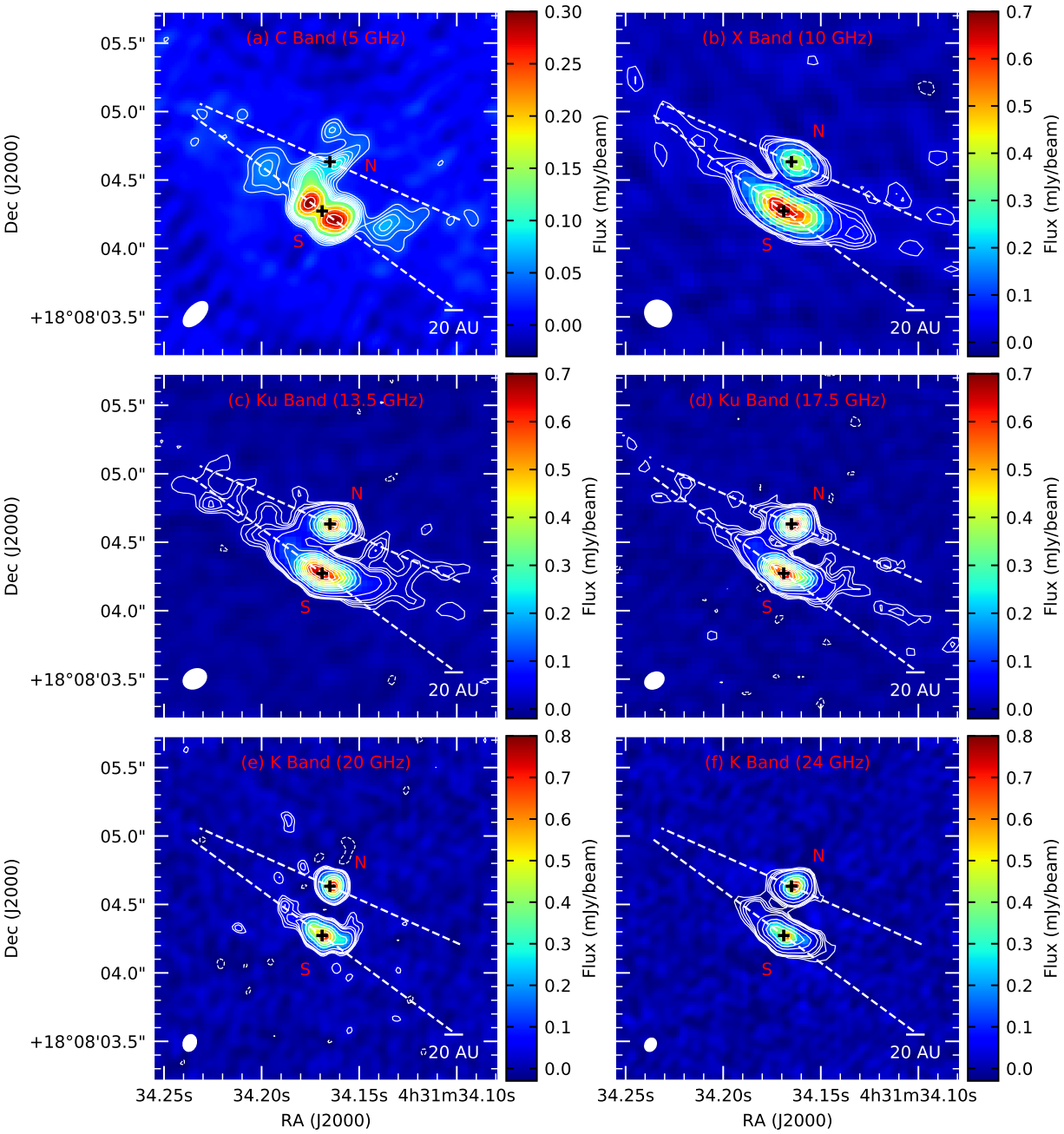

Fig. 1. L1551 IRS 5 from the VLA and e-MERLIN observations (contours + colour scale) as follows: (a) the e-MERLIN + VLA 5 GHz image (b) the VLA 10 GHz image (c) the VLA 13.5 GHz image (d) the VLA 17.5 GHz image (e) the VLA 20 GHz image (f) the VLA 24 GHz image. The black crosses in each image indicate the peaks of the disk emission of the two sources in the ALMA 153 GHz image to show the approximate positions of the central stars. The jet axes of the two components from Rodríguez et al. (2003b) are shown by the dotted white lines. The contour levels in the 5 GHz image are −3, 3, 4, 5, 6, 7, 8, 9, 10, 15, 20, and $25 \times \sigma_{\rm rms}$, where σ_{rms} is the root-mean-square noise of the image. For the 10 GHz, 20 GHz, and 24 GHz images, the contour levels are −3, 3, 4, 5, 6, 10, 20, 30, 40, 50, and $60 \times \sigma_{\rm rms}$. For the 13.5 GHz and 17.5 GHz images, the contour levels are −3, 3, 4, 5, 6, 10, 20, 30, 40, 50, 60, 70, 80, 90, 100, and $110 \times \sigma_{\rm rms}$. The synthesised beam for each image is shown in the bottom left corner. The values for the synthesised beam and $\sigma_{\rm rms}$ of each image are given in Table 3.

jet is constant ($T_{\rm e}(r) = T_0$, $v(r) = v_0$). The spectrum model for the thermal free-free emission is then:

$$\left(\frac{S_\nu}{\rm mJy}\right) = 1.9 \times 10^{-7} \left(\frac{D}{\rm pc}\right)^{-2} \left(\frac{T_{\rm e}}{\rm K}\right)^{1/10} \left(\frac{r_0}{\rm au}\right) \left(\frac{w_0}{\rm au}\right)^{5/3} \left(\frac{n_0}{\rm cm^{-3}}\right)^{4/3} \times (\sin i)^{1/3} \left(\frac{\nu}{\rm GHz}\right)^{0.6} = K_{\rm ff} \left(\frac{\nu}{\rm GHz}\right)^{0.6} \quad (1)$$

where D is the distance to the object and i is the inclination angle of the jet to the line of sight. When fitting the spectrum, all of the non-frequency parameters were combined into the parameter $K_{\rm ff}$ as a constant of proportionality for the free-free emission. We note that this equation is only accurate below the threshold frequency $\nu_{\rm m}$ above which the jet becomes entirely optically thin. However, for typical parameters of a jet this is usually estimated to be $\nu_{\rm m} > 40$ GHz (Anglada et al. 2018), at which point the spectra of the sources are clearly dominated by dust emission.

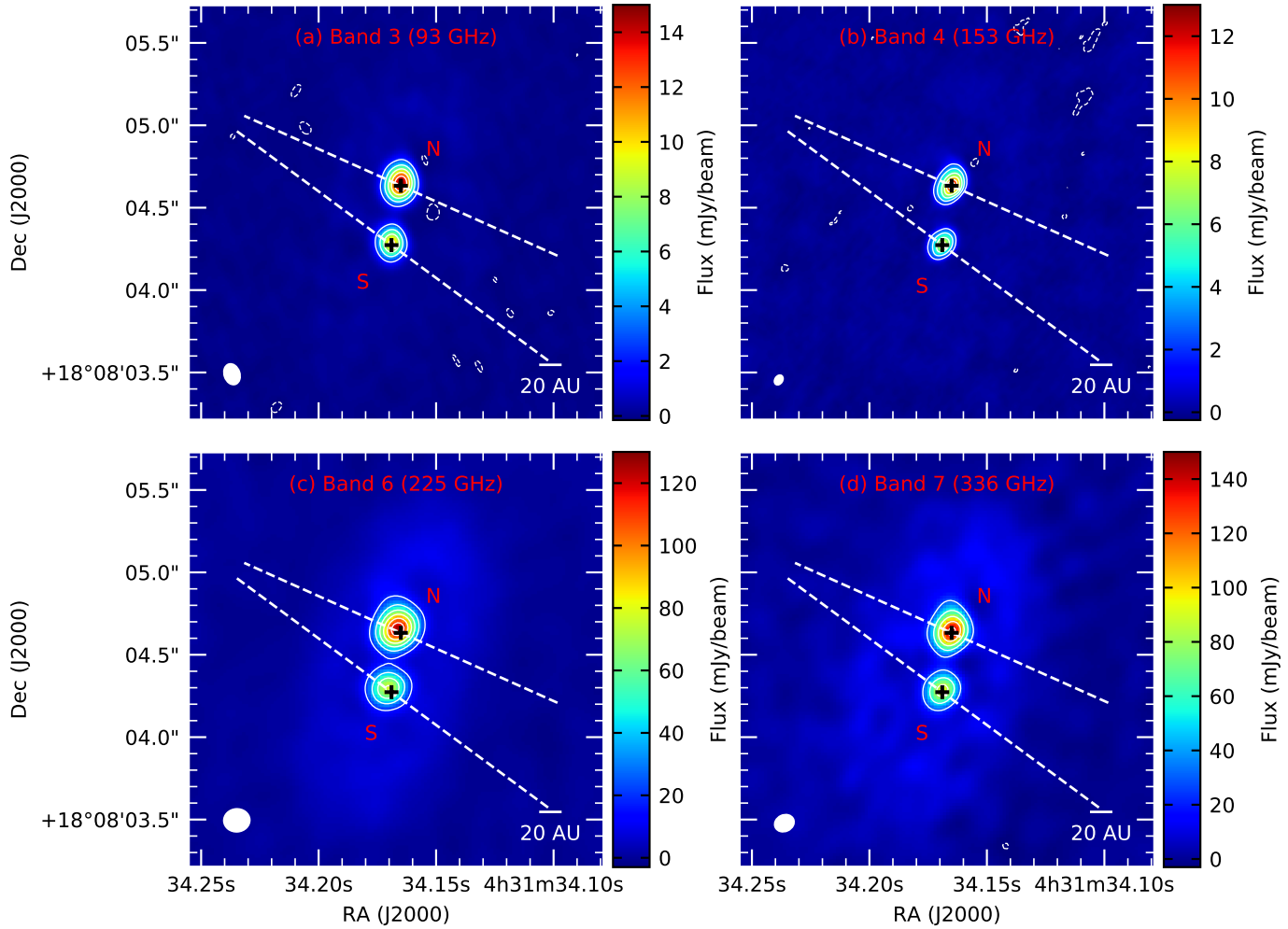

Fig. 2. L1551 IRS 5 from the ALMA observations (contours + colour scale) as follows: (a) the ALMA 93 GHz image (b) the ALMA 153 GHz image (c) the ALMA 225 GHz image (d) the ALMA 336 GHz image. The black crosses in each image indicate the peaks of the disk emission of the two sources in the ALMA 153 GHz image to show the approximate positions of the central stars. The jet axes of the two components from Rodríguez et al. (2003b) are shown by the dotted white lines. The contour levels in the 93 GHz image are −3, 50, 100, 150, 200, 250, and $300 \times \sigma_{\rm rms}$, where $\sigma_{\rm rms}$ is the root-mean-square noise of the image. For the 153 GHz and 225 GHz images, the contour levels are −3, 25, 50, 75, 100, 125, and $150 \times \sigma_{\rm rms}$. For the 336 GHz image, the contour levels are −3, 25, 50, 75, 100, and $125 \times \sigma_{\rm rms}$. The synthesised beam for each image is shown in the bottom left corner. The values for the synthesised beam and $\sigma_{\rm rms}$ of each image are given in Table 3.

The dust emission component was modelled using a simple power-law $S_\nu \propto \nu^\alpha$ giving a total model spectrum of:

$$\left(\frac{S_\nu}{\rm mJy}\right) = K_{\rm ff}\left(\frac{\nu}{\rm GHz}\right)^{0.6} + K_{\rm dust}\left(\frac{\nu}{\rm GHz}\right)^{\alpha_{\rm dust}} \quad (2)$$

where $K_{\rm dust}$ is a constant of proportionality for the dust emission component and $\alpha_{\rm dust}$ is the spectral index of the dust emission.

The S component was fit very well by this, as seen in Fig. 5, with the flux density at low frequencies being mainly due to free-free emission and at higher frequencies being mainly due to dust emission with a spectral index for the dust emission of $\alpha_{\rm dust}$ = 2.4±0.3. In the N component, the data were fit well by the model, as seen in Fig. 5. However, the fit seems to suggest that there is almost no free-free emission present and the emission is almost entirely due to dust emission with a spectral index of $\alpha_{\rm dust}$ = 2.05 ± 0.07. Although in the Ku Band images of L1551 IRS 5 shown in Fig. 1, there is clearly some emission seen along the jet axis of the N component, indicating that there is at least some level of free-free emission from the jet present.

For L1551 NE, we do not have as many data points as for L1551 IRS 5, particularly at higher frequencies where we only have ALMA observations in one band. However, it can still be seen in Fig. 6 that the spectra for both components A and B can be fit well by a combination of thermal free-free emission and dust emission, with free-free emission dominant at lower frequencies and dust emission dominant at higher frequencies. The spectral indices for the dust component are $\alpha_{\rm dust}$ = 2.13 ± 0.04 and $\alpha_{\rm dust}$ = 2.4 ± 0.2 for components A and B respectively.

4.2. Morphology

When comparing the *C* Band image of L1551 IRS 5 shown in Fig. 1a with previous images at centimetre wavelengths from Rodríguez et al. (1998, 2003b), it is clear that there are significant changes in the morphology of the jets of both sources. For example, there are two strong emission knots seen along the jet axis of the N component in the image from Rodríguez et al. (2003b), one to the north-east and one to the south-west. However, these seem to have disappeared in the images that we obtained. This is not that surprising when considering the proper motion of the

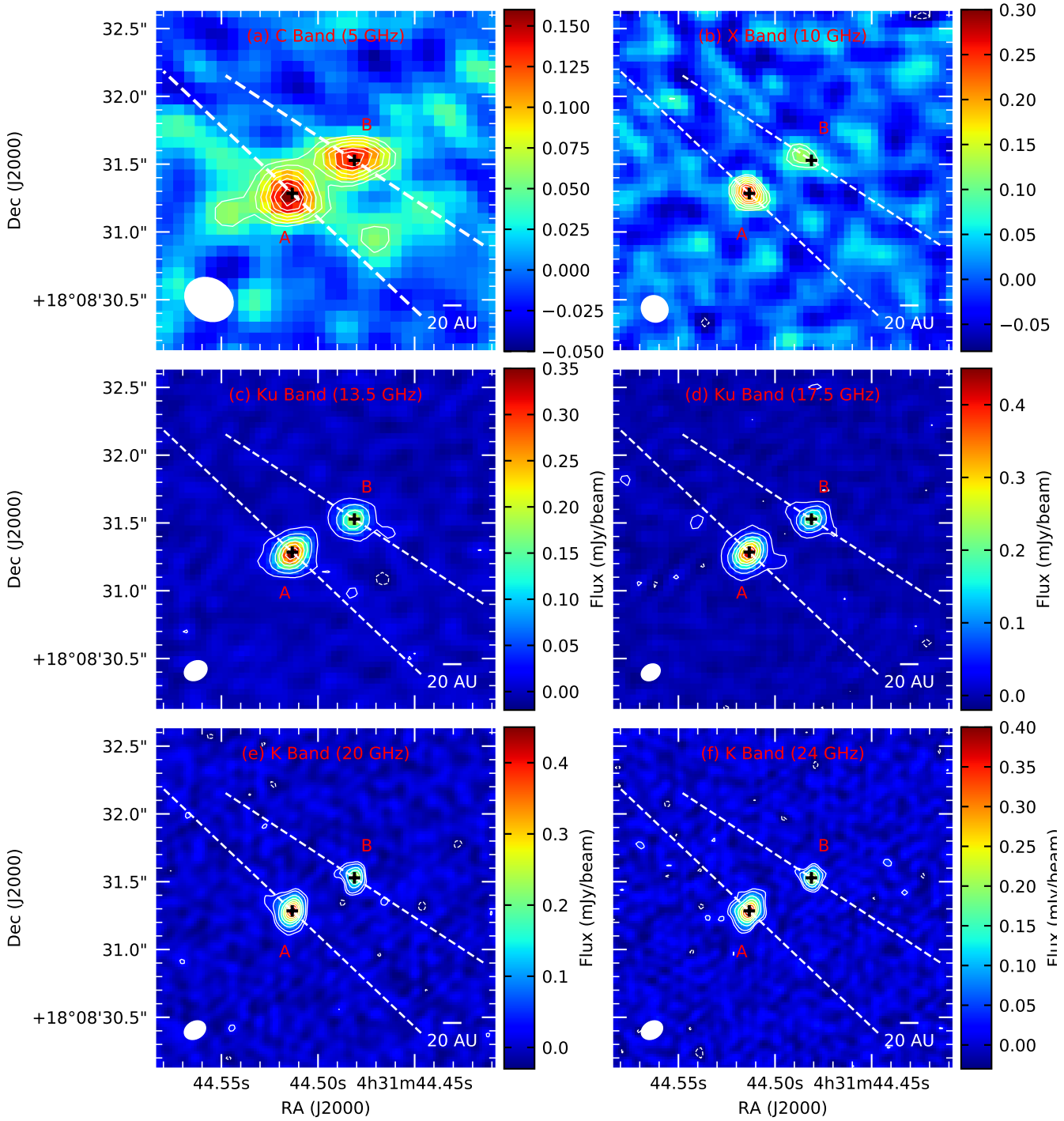

Fig. 3. L1551 NE from the VLA observations (contours + colour scale) as follows: (a) the VLA 6 GHz image. (b) the VLA 10 GHz image (c) the VLA 13.5 GHz image (d) the VLA 17.5 GHz image (e) the VLA 20 GHz image (f) the VLA 24 GHz image. The black crosses in each image indicate the peaks of the disk emission of the two sources in the 24 GHz image to show the approximate positions of the central stars. The jet axes of the two components from Reipurth et al. (2002) are shown by the dotted white lines. The contour levels in the 6 GHz image are −3, 3, 4, 5, 6, 7, 8, and $9 \times \sigma_{\rm rms}$, where $\sigma_{\rm rms}$ is the root-mean-square noise of the image. For the 10 GHz image, the contour levels are −3, 3, 4, 5, 6, 7, 8, 9, and $10 \times \sigma_{\rm rms}$. For the 13.5 GHz and 17.5 GHz images, the contour levels are −3, 3, 10, 20, 30, 40, 50, and $60 \times \sigma_{\rm rms}$. For the 20 GHz image, the contour levels are −3, 3, 5, 10, 15, 20, 25, 30, 35, and $40 \times \sigma_{\rm rms}$. For the 24 GHz image, the contour levels are −3, 3, 5, 10, 15, 20, 25, 30, and $35 \times \sigma_{\rm rms}$. The synthesised beam for each image is shown in the bottom left corner. The values for the synthesised beam and $\sigma_{\rm rms}$ of each image are given in Table 4.

material in the jet. Anglada et al. (2018) estimated a jet velocity of $v_{\rm jet} \sim 150\,{\rm km\,s^{-1}}$ for L1551 IRS 5. This would give a proper motion of ∼150 mas yr^{-1} at a distance of 147 pc with an inclination of $i = 45°$. Since the Rodríguez et al. (2003b) observations were taken in February 2002, this would give ∼2.6″, or ∼400 au, of proper motion between the two epochs. In addition, the emission from any ejected material is likely to decline with time as it moves outwards along the jet due to recombination of the ionised material and decreasing electron density. The recombination time for the ionised material in the jet is given by $t = 1/(n_{\rm e}\alpha)$,

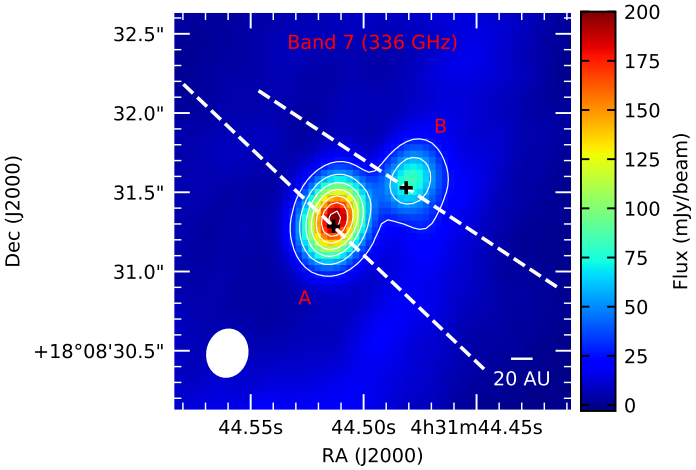

Fig. 4. L1551 NE from the 336 GHz ALMA observation (contours + colour scale). The black crosses in the image indicate the peaks of the disk emission of the two sources in the 24 GHz image to show the approximate positions of the central stars. The jet axes of the two components from Reipurth et al. (2002) are shown by the dotted white lines. We note that there is a displacement between the peaks of the ALMA 336 GHz image and the 24 GHz image due to proper motion of the source between the epochs (Oct. 2019 and Jan. 2021) which was not corrected for in the image. The contour levels are −3, 25, 50, 75, 100, 125, 150, and $175 \times \sigma_{\rm rms}$, where $\sigma_{\rm rms}$ is the root-mean-square noise of the image. The synthesised beam for the image is shown in the bottom left corner. The values for the synthesised beam and $\sigma_{\rm rms}$ are given in Table 4.

where α is the recombination rate. For hydrogen, the recombination rate at $T = 10^4$ K is typically $\alpha = 4.16 \times 10^{-13}$ s^{-1} cm^3 (Pradhan & Nahar 2011). Consider an emission knot in the jet of the N component at a distance of ∼100 au from the star. From the ionised mass-loss rate measured in Sect. 4.4 and $q_n = -2$ we can estimate an electron density of $n_{\rm e} \sim 10^4$ cm^{-3} at this distance in the jet. This would imply a recombination time of ∼7.6 yr. From this, it is clear that most of the ionised material in any emission knot can recombine between the two epochs and therefore the thermal emission would disappear.

One thing of interest is that in Rodríguez et al. (2003b), they detected a region of emission between the two jets ∼0.6″ to the south-west of the two sources. They speculated that this emission could be due to a region of shock interaction between the outer parts of the outflows. They stated that to test this hypothesis, a lack of proper motion would have to be observed in this emission as an interaction zone between the two outflows should remain stationary. In Figs. 1a and b, a region of emission is also detected between the outflows to the south-west of the two sources at a similar position to that of the emission detected by Rodríguez et al. (2003b). If this emission corresponds to the same emission region as the one they detected, this would indicate a lack of proper motion and back up their hypothesis of this being a region of shock interaction between the two outflows.

4.3. Flux variability

Variability in the flux density of L1551 IRS 5 can clearly be seen looking at the spectra in Fig. 5 and comparing the flux densities in this work with those from Rodríguez et al. (1998), observed between 1985 and 1997, and from Rodríguez et al. (2003b), observed in 2002. It is clear that there is a high degree of variability in the jet emission of both sources, as the flux density at lower frequencies ($\nu \lesssim 20$ GHz), where the jet emission dominates, varies significantly between the three epochs. On the other hand, the flux density at higher frequencies ($\nu \gtrsim 20$ GHz), where the disk emission dominates, is similar at both epochs, indicating that the disk emission has not varied significantly. In the N component in particular, the flux density has decreased significantly by a factor of ∼5 at 5 GHz compared with the data in Rodríguez et al. (1998). This suggests that the free-free emission from the jet has drastically decreased between the two epochs. The S component on the other hand, shows more modest although still significant variability between the two epochs with an increase in flux density by a factor of ∼2 at 5 GHz. The synthesised beam sizes are similar in all of the observations, with beam sizes of 0.″25×0.″24 and 0.″18×0.″12 in the Rodríguez et al. (1998, 2003b) 8.3 GHz observations respectively, compared with 0.″20 × 0.″18 in the 5 GHz observation in this work, and so the differences in flux density are unlikely to be due to differences in the scales of emission being recovered.

For L1551 NE, the flux densities obtained from this work can be compared with the data from Reipurth et al. (2002), observed in 2000, as shown in Fig. 6. The synthesised beam size is similar for both epochs, 0.″37 × 0.″30 in our observations vs 0.″34 × 0.″27 in Reipurth et al. (2002), and so they should recover similar scales of emission. While Reipurth et al. (2002) only observed L1551 NE at one frequency, it can still be seen that the flux density at low frequencies seems to have decreased in both components at 8 GHz between 2000 and 2021, with the flux density in component B decreasing by a factor of ∼2. This would indicate that the free-free emission from the jet has decreased in both components.

This level of flux variability, particularly for the N component of L1551 IRS 5, where the free-free emission seems to have almost disappeared, is quite remarkable. For most YSOs observed, the free-free emission shows only modest variability of the order of 10−20% (e.g. Rodríguez et al. 2008, 2014; Carrasco-González et al. 2012). The variability observed in L1551 IRS 5 and L1551 NE suggests that binary systems could show more temporal changes in their ionised mass loss rate than single sources. However, a few cases of extreme variability have been seen previously in presumably single stars. For example, the flux density of the radio jet in B335 was found to increase by a factor of ≳5 between 1994 and 2000 (Avila et al. 2001; Reipurth et al. 2002) while DG Tau A showed an increase in flux density by a factor of ∼2 between 1994 and 1996 (Rodríguez et al. 2012). Interestingly, Gâlfalk & Olofsson (2007) proposed that B335 could be a binary system. Additional studies of variability and multiplicity are needed to investigate this issue.

4.4. Ionised mass-loss rate

From the fit to the spectra of the sources, the ionised mass-loss rates of the jets could be estimated. From Reynolds (1986), the ionised mass-loss rate for a conical jet is given by:

$$\left(\frac{\dot{M}_{\rm ion}}{M_\odot\ {\rm yr}^{-1}}\right) = 1.23 \times 10^{-16}\, K_{\rm ff}^{3/4} \theta_0^{3/4} \left(\frac{v}{{\rm km\ s}^{-1}}\right)\left(\frac{D}{\rm pc}\right)^{3/2} \times \left(\frac{T_{\rm e}}{\rm K}\right)^{-0.075} (\sin(i))^{-1/4} \quad (3)$$

where θ_0 is the opening angle of the jet. In addition to getting the ionised mass-loss rate based on our data, we could fit the data from Rodríguez et al. (1998) with the same model to get

Table 3. Flux density measurements in L1551 IRS 5 N component and S component.

ν (GHz)	L1551 IRS 5 N (mJy)	L1551 IRS 5 S (mJy)	$\sigma_{\rm rms}$ (μJy beam^{-1})	Synthesised beam
5	0.11 ± 0.02	1.16 ± 0.07	11	0.″22 × 0.″11, −44°
10	0.47 ± 0.03	1.8 ± 0.1	10	0.″20 × 0.″18, 49°
13.5	0.88 ± 0.05	2.0 ± 0.1	6	0.″17 × 0.″13, −62°
17.5	1.15 ± 0.06	2.1 ± 0.1	6	0.″14 × 0.″11, −59°
20	1.23 ± 0.07	2.1 ± 0.1	12	0.″12 × 0.″09, −18°
24	1.60 ± 0.09	2.1 ± 0.1	12	0.″094 × 0.″074, −29°
93	32 ± 2	18 ± 1	50	0.″124 × 0.″089, 19°
153	79 ± 4	43 ± 2	76	0.″058 × 0.″041, −33°
225	240 ± 10	125 ± 7	750	0.″15 × 0.″13, −85°
336	420 ± 20	210 ± 10	1100	0.″12 × 0.″10, −65°

Table 4. Flux density measurements in L1551 NE component A and component B.

ν (GHz)	L1551 NE A (mJy)	L1551 NE B (mJy)	$\sigma_{\rm rms}$ (μJy beam^{-1})	Synthesised beam
6	0.18 ± 0.03	0.16 ± 0.02	16	0.″37 × 0.″30, 61°
10	0.31 ± 0.04	0.15 ± 0.03	26	0.″20 × 0.″18, 49°
13.5	0.58 ± 0.04	0.27 ± 0.02	6	0.″17 × 0.″13, −61°
17.5	0.81 ± 0.05	0.33 ± 0.02	6	0.″14 × 0.″11, −59°
20	1.11 ± 0.07	0.43 ± 0.03	11	0.″10 × 0.″09, −14°
24	1.36 ± 0.08	0.51 ± 0.04	11	0.″084 × 0.″073, −27°
336	330 ± 20	132 ± 8	1100	0.″30 × 0.″25, −12°

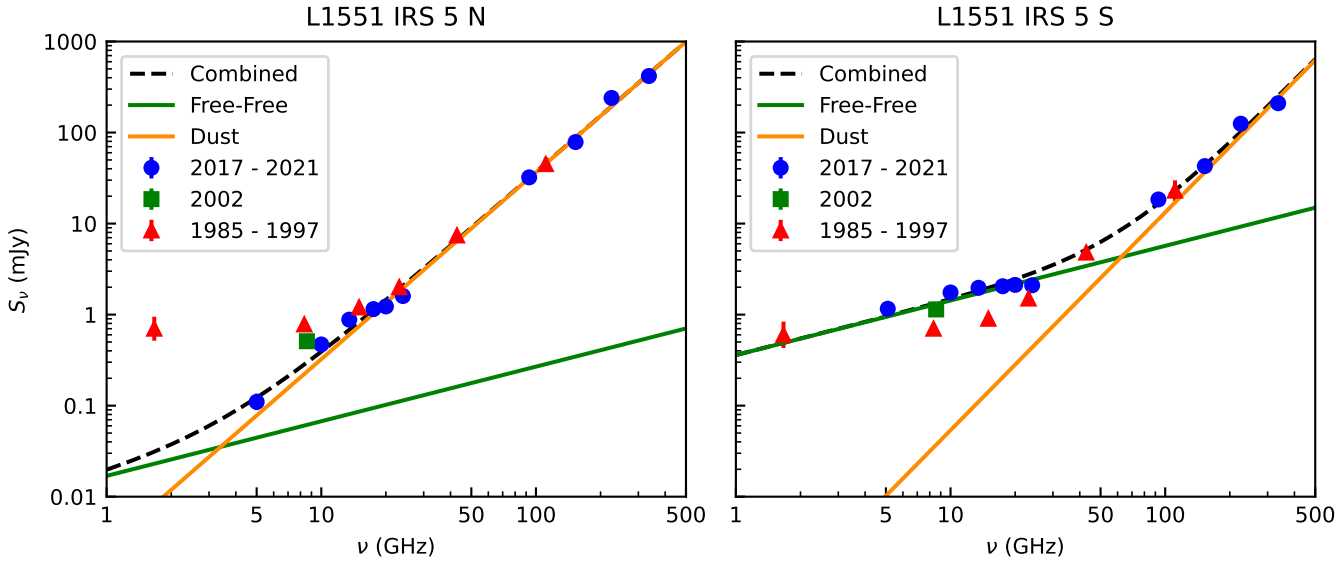

Fig. 5. Spectra of the N component (left) and the S component (right) of L1551 IRS 5 including the total flux density values from this work obtained in 2017–2021 (blue circles), from Rodríguez et al. (2003b) obtained in 2002 (green square), and from Rodríguez et al. (1998) obtained in 1985–1997 (red triangles). The spectra of the 2017–2021 data in both panels were fitted with a combination of free-free emission from the jet (green line) and dust emission from the disk (orange line). The combined fits are shown by the dashed black lines.

the values for a different epoch and compare it with the epoch of this work.

The values obtained for the ionised mass-loss rates in each of the jets in each epoch are listed in Table 5 along with the values of the parameters of Eq. (3) used when deriving the values. For this work, an electron temperature of $T_{\rm e} \sim 10^4$ K was assumed for all of the sources. We note that while the mass-loss rate derived depends on the value of $T_{\rm e}$ assumed, changing the value of $T_{\rm e}$ does not significantly affect the result, as $\dot{M}_{\rm ion}$ is only weakly dependent on $T_{\rm e}$ ($\dot{M}_{\rm ion} \propto T_{\rm e}^{0.075}$). A rough estimate for the opening angle can be found from the deconvolved major and minor axis of the jet emission: $\theta_0 \approx 2\tan^{-1}(\theta_{\rm min}/\theta_{\rm maj})$. For L1551 IRS 5, using the values of $\theta_{\rm min}$ and $\theta_{\rm maj}$ obtained by Rodríguez et al. (2003b), this gave estimates of $\theta_0 \approx 43°$

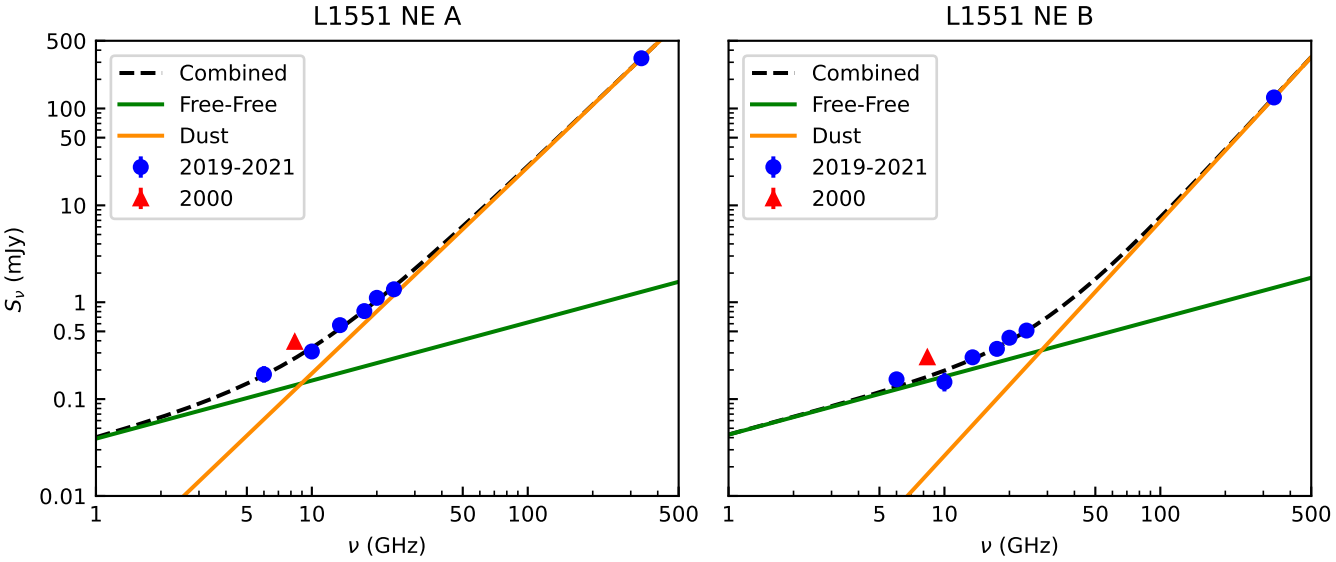

Fig. 6. Spectra of component A (left) and component B (right) of L1551 NE including the total flux density values from this work obtained in 2019–2021 (blue circles) and the values from Reipurth et al. (2002) obtained in 2000 (red triangle). The spectra of the 2019–2021 data in both panels were fitted with a combination of free-free emission from the jet (green line) and dust emission from the disk (orange line). The combined fits are shown by the dotted black lines.

Table 5. Ionised mass-loss rates of L1551 IRS 5 and L1551 NE radio jets.

Source	Epoch	$K_{\rm ff}$ (mJy)	θ_0	v (km s^{-1})	D (pc)	$T_{\rm e}$ (K)	i	$\dot{M}_{\rm ion}$ ($M_\odot$ yr^{-1})
L1551 IRS 5 N	1985–1997	0.29 ± 0.09	0.75	150	147	10^4	45	$(5.3 \pm 1.2) \times 10^{-9}$
	2017–2021	0.017 ± 0.013	0.75	150	147	10^4	45	$(0.6 \pm 0.4) \times 10^{-9}$
L1551 IRS 5 S	1985–1997	0.24 ± 0.07	0.49	150	147	10^4	45	$(3.4 \pm 0.8) \times 10^{-9}$
	2017–2021	0.36 ± 0.04	0.49	150	147	10^4	45	$(4.5 \pm 0.4) \times 10^{-9}$
L1551 NE A	2019–2021	0.039 ± 0.006	0.52	160	147	10^4	58	$(1.0 \pm 0.1) \times 10^{-9}$
L1551 NE B	2019–2021	0.043 ± 0.007	0.52	70	147	10^4	58	$(0.5 \pm 0.1) \times 10^{-9}$

and $\theta_0 \approx 28°$ for the N and S component respectively. For L1551 NE, neither our observations nor the observations from Reipurth et al. (2002) had sufficient resolution to estimate the major and minor axes of the jet. Therefore, we used a reasonable estimate of $\theta_0 \approx 30°$ for these jets. For the jet velocity, the value for L1551 IRS 5 from Anglada et al. (2018) was used, while for L1551 NE, Eq. (12) from Anglada et al. (2018) was used to obtain rough estimates of v for the two components based on the stellar masses of the sources, which are $M_{\rm A} \sim 0.67\,M_\odot$ and $M_{\rm B} \sim 0.13\,M_\odot$ respectively (Takakuwa et al. 2012, 2014).

For the N component of L1551 IRS 5, it can be seen that there has been a factor of ∼10 decrease in the ionised mass-loss rate of the jet between 1998 and 2020. While in the S component, there has been a small increase in the ionised mass-loss rate of the jet between the two epochs. Such changes are of course to be expected based on the change in flux density. We note that while these changes in the ionised mass-loss rates are likely due to changes in the total mass-loss rate of the jets, they could also be due to changes in the ionisation fractions of the jets.

We can compare the values of $\dot{M}_{\rm ion}$ estimated with the total mass-loss rate of L1551 IRS 5 to obtain values for the ionisation fraction of the jets. Based on SOFIA observations of [O I]$_{63}$ emission from 2019, Sperling et al. (2021) calculated the mass-loss rate of the atomic jet of L1551 IRS 5. They determined that the [O I]$_{63}$ emission in L1551 IRS 5 can be described by the Hollenbach & McKee (1989) shock model, which predicts that the [O I]$_{63}$ emission is produced in dissociative J-shocks in the jet. Applying this model to L1551 IRS 5, they estimated, based on the luminosity of the [O I]$_{63}$ emission, that the mass-loss rate is $4.9–5.4 \times 10^{-7}\,M_\odot$ yr^{-1}. By comparing this with mass-loss rate estimates based on other atomic and molecular emission lines, they determined that the atomic component is the dominant component of the jet. Therefore, this estimate for the mass-loss rate of the atomic component should provide a good estimate for the total mass-loss rate of the jet of L1551 IRS 5. Unfortunately, the two individual jets are unresolved and so we only have the total mass-loss rate for the whole system. But using this value as an upper limit for the total mass-loss rate in each jet gives an estimate for the ionisation fraction in each jet of $\gtrsim$0.1% and $\gtrsim$1% for the N and S components respectively. This ionisation level can be readily produced by an X-wind model (e.g. Shang et al. 2004) with the mass loss rates inferred. However, these are only rough estimates for the ionisation fractions given the large errors involved.

For L1551 NE, we could not calculate the previous ionised mass-loss rate from a fit to the spectrum as Reipurth et al. (2002) only observed the source at one frequency. However, from this measurement there appears to have been a decrease of a factor of ∼2 in flux between 2000 and 2021 in the free-free portion of the spectra of the components. Based on this, we can infer that there

has likely been a decrease in the free-free emission of the jets and therefore a decrease in the ionised mass-loss rates of both of the jets.

4.5. Radiative transfer modelling

In order to better understand the properties of the jet, radiative transfer modelling was performed for the jet in the S component of L1551 IRS 5 using the package *sf3dmodels* (Izquierdo et al. 2018) to model the jet and RADMC-3D (Dullemond et al. 2012) to then perform the radiative transfer calculations. *sf3dmodels* creates a three-dimensional (3D) grid of the temperature, ionisation fraction, and density of the jet based on the model of Reynolds (1986). This allows us to obtain estimates for the injection radius r_0, that is at what distance above the disk the ionised flow in the jet begins, as well as the ionised mass-loss rate $\dot{M}_{\rm ion}$. To create this model, values for $\dot{M}_{\rm ion}$, r_0, the velocity of the jet v_0, electron temperature $T_{\rm e}$, half-width at the base of the jet w_0, and inclination angle i of the jet are required. The model of an ionised, conical jet from Reynolds (1986) was used again, with $\epsilon = 1$, $q_n = -2\epsilon = -2$, and a constant temperature and velocity in the jet. The jet was modelled out to a distance of 120 au from the star and the resolution of the 3D grid was 0.25 au.

Once the physical models were generated, RADMC-3D was used to solve the equation of radiative transfer for free-free emission to generate a synthetic image of the region at a given wavelength. For L1551 IRS 5, we simulated images at 5 GHz and 10 GHz, since at these frequencies almost all of the emission should be free-free emission as opposed to dust emission and so it should be possible to replicate the observed image using only free-free emission. The model images created were convolved with the same synthesised beam as the observed image of the same frequency in order to compare the two. We aimed to recreate the jet morphology, that is the double lobe structure in the 5 GHz image, and the flux density seen in the observed images as best we could. To assess the accuracy of the model images, residual images were also generated by subtracting the model images from the observed images.

When creating the model, an estimate for the jet velocity of $v_0 = 150\,{\rm km\,s^{-1}}$ and a temperature of $T_{\rm e} = 10^4$ K was used. The half-width w_0 was taken to be given by r_0 and the opening angle of the jet $\theta_0 = 2(w_0/r_0)$. The morphology of the jet in the image was then mainly adjusted using the input value for r_0, while the flux density was adjusted using the value for $\dot{M}_{\rm ion}$.

It was found that the observed jet was best reproduced using values of $r_0 \approx 10$ au and $\dot{M}_{\rm ion} \approx 4.3 \times 10^{-9}\,M_\odot\,{\rm yr^{-1}}$. This can be seen and compared with the observed image in Fig. 7. We note that the ionised mass-loss rate obtained is nearly the same as that predicted by Eq. (3). It can be seen the model images reproduce the observed images quite well, as the double lobe structure in the 5 GHz image is observed and the flux densities are similar. This can also be seen in the residual images, as most of the observed emission has been subtracted. Although in both the 5 GHz and 10 GHz images, there is some emission to the south-west of the source in the blue-shifted jet which is still present in the residuals. This is likely as the jet is asymmetric, which was not accounted for in the model.

The models obtained for the 5 GHz and 10 GHz emission both predict that the free-free emission flux density should consist of two peaks on either side of the central star, with the emission then declining along the jet axis. However, when the images were convolved with the synthesised beams of the observed images, it can be seen that while in the 5 GHz image two peaks are seen, in the 10 GHz image the two peaks were not resolved. Instead, the emission is elongated with a peak at the position of the central star. This is due mainly to the lower angular resolution along the jet axis in the 10 GHz image. In addition, the optical depth at higher frequencies is lower and so the peaks of the emission are closer together.

The value obtained for r_0 could be interpreted as being due to variability in the mass loss rate of the jet. If the two lobes represent a recent increase in the ionised mass-loss rate followed by a decrease, this would explain the lack of emission closer to the origin of the jet. This would also be consistent with knots along the jet being due to variations in mass-loss-rate. For $r_0 \approx 10$ au and a velocity of $v_0 = 150\,{\rm km\,s^{-1}}$, this would indicate variations in the mass-loss rate of the jet on timescales of ∼4 months. Alternatively, it could be the case that the material in the jet is only ionised at a distance of 10 au, possibly due to a shock in the jet, or a new ionising event due to variability. As a result, there would be no ionised material closer to the origin of the jet.

These results have implications for the study of the jet launching mechanism, as any model of jet generation such as the X-wind model or the disk wind model, would need to explain the double lobe structure observed and the value of r_0 obtained for L1551 IRS 5 S. For example, through the jet being ionised at a shock front at a distance of r_0 or through mass-loss rate variability on timescales of a few months. In magnetocentrifugal wind models, the Alfvén radii are much smaller than where the jet self-collimates. The strong ionisation and high density from the jet axis out to the jet half-width w_0 provide constraints on the wind launching mechanism. In particular, the observed jet velocity, high ionisation, and the inferred high ionised jet density from the axis to w_0 are normal characteristics of the X-wind model, where the wind is launched from a radius much smaller than w_0 (e.g. Shang et al. 2002, 2004). For L1551 IRS 5 S, the jet width w_0 was found to be 2.5 au, based on $\theta_0 = 0.49$, and $r_0 = 10$ au. Furthermore, the high jet velocity of $v_0 \sim 150\,{\rm km\,s^{-1}}$ implies a launch radius $\lesssim$0.2 au, which is the innermost region of the disk.

Finally, our results also show the importance of high-resolution observations of free-free emission from radio jets, particularly at lower frequencies (∼5 GHz) where dust emission is negligible. By comparing the observations with simulations, we were able to probe the jet launching and collimation regions.

5. Conclusions

L1551 IRS 5 and L1551 NE were successfully imaged at a wide range of frequencies using high spatial resolution observations with e-MERLIN, the VLA, and ALMA. In particular, the 5 GHz image of L1551 IRS 5 that was obtained is one of the highest-resolution images of a radio jet from a low-mass YSO obtained to date, with emission resolved on a scale of only ∼15 au. Emission was detected from all of the components of the two binary systems at all frequencies. By plotting and fitting the spectra of the sources, it is apparent that free-free emission dominates at lower frequencies while dust emission dominates at higher frequencies, as expected. Although, for the N component of L1551 IRS 5, there appears to be very little free-free emission present.

Significant changes in morphology and high levels of variability in flux density were seen in both components of L1551 IRS 5. In particular, the N component of L1551 IRS 5 appears to have declined in flux density by a factor of ∼5 at lower frequencies, suggesting that the free-free emission of this source has almost disappeared.

From fitting the spectra, estimates for the ionised mass-loss rates of each source were derived. By comparing the values

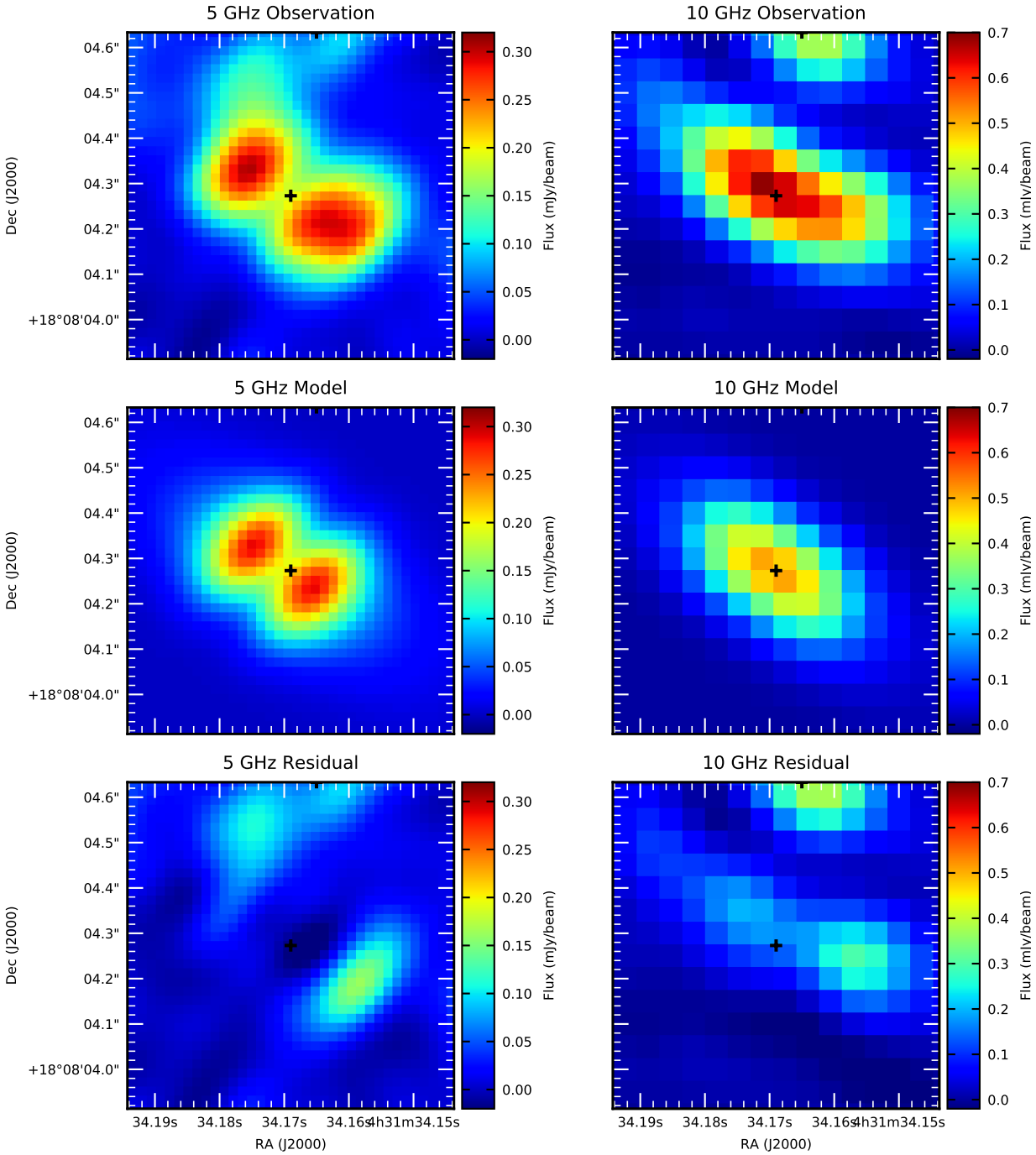

Fig. 7. VLA+e-MERLIN 5 GHz image (left) and VLA 10 GHz image (right) of the S component of L1551 IRS 5 compared with the images obtained from radiative transfer modelling (middle) and with the residual images obtained by subtracting the model images from the observed images (bottom). The peak of the emission in the ALMA 153 GHz image is indicated by the black cross to show the approximate position of the central star.

obtained to an estimate for the total mass-loss rate based on atomic line observations, it was estimated that the ionisation fractions of the jets in L1551 IRS 5 are of the order of $\gtrsim$0.1% and $\gtrsim$1% for the N and S components, respectively.

Given the variability in flux density of the free-free emission of the jets, this implied there is variability in their ionised mass-loss rates. By comparing the mass-loss rates derived based on the data in this work and from a previous epoch, it was shown that there is significant variation in the ionised mass-loss rate of the jets, particularly the N component of L1551 IRS 5, on timescales of several years. This indicates that there has been either significant changes in the total mass-loss rates of the jets or, alternatively, changes in the ionisation fraction of the jets.

The high resolution and sensitivity achieved in the 5 GHz image of L1551 IRS 5 made it possible to study the inner region of the radio jet of the S component in detail. By creating a physical model and then using radiative transfer modelling to create a simulated image that could be compared with the observed image, it was possible to obtain an estimate for the injection radius and ionised mass-loss rate of the jet of $r_0 \approx 10$ au and $\dot{M}_{\rm ion} \approx 5.7 \times 10^{-9}\,M_\odot\,{\rm yr}^{-1}$, respectively. The strong ionisation and high density from the jet axis to its width, $w_0 \approx 2.5$ au, support the

normal characteristics of an X-wind model. The high jet velocity of $v_0 \sim 150\,\mathrm{km\,s^{-1}}$ suggests that the underlying magnetocentrifugal wind comes from the innermost 0.2 au or smaller. It is very difficult to produce these findings by a disk wind. Our data and the modelling analysis thus favour the X-wind model.

These results show the use of high-resolution, high-sensitivity radio and millimetre observations for the study of radio jets from YSOs. Future ultra-sensitive interferometers such as the Square Kilometer Array (SKA) or the Next-Generation Very Large Array (ngVLA) will allow for many more YSOs to be studied in this way and potentially help us learn more about the innermost regions of protostellar jets.

Acknowledgements. A.F.J., S.J.D.P. and T.P.R. acknowledge funding from the European Research Council (ERC) under Advanced Grant No. 743029. A.F.J. also acknowledges support from NAOJ ALMA Scientific Research Grant code 2019-13B. C.C.-G. and R.G.M. acknowledge support from UNAM DGAPA-PAPIIT grants IN108822 and IG101321 as well as from CONACyT Ciencia de Frontera project ID 86372. A.R.-K. thanks the UNAM DGAPA Postdoctoral Fellowship Program. S.L. acknowledges support from UNAM-PAPIIT grant IN103921.

References

Anglada, G., Rodríguez, L. F., & Carrasco-González, C. 2018, A&ARv, 26, 3
Audard, M., Ábrahám, P., Dunham, M. M., et al. 2014, in Protostars and Planets VI, eds. H. Beuther, R. S. Klessen, C. P. Dullemond, & T. Henning (Tucson: University of Arizona Press), 387
Avila, R., Rodríguez, L. F., & Curiel, S. 2001, Rev. Mex. Astron. Astrofis., 37, 201
Bacciotti, F., Ray, T. P., Mundt, R., Eisloffel, J., & Solf, J. 2002, ApJ, 576, 222
Blandford, R. D., & Payne, D. G. 1982, MNRAS, 199, 883
Carrasco-González, C., Osorio, M., Anglada, G., et al. 2012, ApJ, 746, 71
Carrasco-González, C., Sierra, A., Flock, M., et al. 2019, ApJ, 883, 71
Carrasco-González, C., Sanna, A., Rodríguez-Kamenetzky, A., et al. 2021, ApJ, 914, L1
CASA Team (Bean, B., et al.) 2022, PASP, 134, 114501
Chou, T.-L., Takakuwa, S., Yen, H.-W., Ohashi, N., & Ho, P. T. P. 2014, ApJ, 796, 70
Connelley, M. S., & Reipurth, B. 2018, ApJ, 861, 145
Cruz-Sáenz de Miera, F., Kóspál, Á., Ábrahám, P., Liu, H. B., & Takami, M. 2019, ApJ, 882, L4
Curiel, S., Canto, J., & Rodriguez, L. F. 1987, Rev. Mex. Astron. Astrofis., 14, 595
Dullemond, C. P., Juhasz, A., Pohl, A., et al. 2012, Astrophysics Source Code Library [record ascl:1202.015]
Frank, A., Ray, T. P., Cabrit, S., et al. 2014, in Protostars and Planets VI, eds. H. Beuther, R. S. Klessen, C. P. Dullemond, & T. Henning (Tucson: University of Arizona Press), 451
Gâlfalk, M., & Olofsson, G. 2007, A&A, 475, 281
Hollenbach, D., & McKee, C. F. 1989, ApJ, 342, 306
Izquierdo, A. F., Galván-Madrid, R., Maud, L. T., et al. 2018, MNRAS, 478, 2505
Lim, J., & Takakuwa, S. 2006, ApJ, 653, 425
Lim, J., Hanawa, T., Yeung, P. K. H., et al. 2016a, ApJ, 831, 90
Lim, J., Yeung, P. K. H., Hanawa, T., et al. 2016b, ApJ, 826, 153
Liseau, R., Fridlund, C. V. M., & Larsson, B. 2005, ApJ, 619, 959
Mundt, R., & Fried, J. W. 1983, ApJ, 274, 83
Pradhan, A. K., & Nahar, S. N. 2011, Atomic Astrophysics and Spectroscopy (Cambridge: Cambridge University Press)
Pudritz, R. E., & Norman, C. A. 1983, ApJ, 274, 677
Ray, T. P., & Ferreira, J. 2021, New Astron. Rev., 93, 101615
Reipurth, B., Rodríguez, L. F., Anglada, G., & Bally, J. 2002, AJ, 124, 1045
Reynolds, S. P. 1986, ApJ, 304, 713
Rodríguez, L. F., D'Alessio, P., Wilner, D. J., et al. 1998, Nature, 395, 355
Rodríguez, L. F., Curiel, S., Canto, J., et al. 2003a, ApJ, 583, 330
Rodríguez, L. F., Porras, A., Claussen, M. J., et al. 2003b, ApJ, 586, 137
Rodríguez, L. F., Moran, J. M., Franco-Hernández, R., et al. 2008, AJ, 135, 2370
Rodríguez, L. F., González, R. F., Raga, A. C., et al. 2012, A&A, 537, A123
Rodríguez, L. F., Zapata, L. A., Dzib, S. A., et al. 2014, ApJ, 793, L21
Rodríguez-Kamenetzky, A. R., Carrasco-González, C., Rodríguez, L. F., et al. 2022, ApJ, 931, L26
Shang, H., Glassgold, A. E., Shu, F. H., & Lizano, S. 2002, ApJ, 564, 853
Shang, H., Lizano, S., Glassgold, A., & Shu, F. 2004, ApJ, 612, L69
Shu, F., Najita, J., Ostriker, E., et al. 1994, ApJ, 429, 781
Snell, R. L., Loren, R. B., & Plambeck, R. L. 1980, ApJ, 239, L17
Sperling, T., Eislöffel, J., Fischer, C., et al. 2021, A&A, 650, A173
Takakuwa, S., Saito, M., Lim, J., et al. 2012, ApJ, 754, 52
Takakuwa, S., Saito, M., Saigo, K., et al. 2014, ApJ, 796, 1
Takakuwa, S., Saigo, K., Matsumoto, T., et al. 2017, ApJ, 837, 86
Takakuwa, S., Saigo, K., Matsumoto, T., et al. 2020, ApJ, 898, 10
Villa, A. M., Trinidad, M. A., de la Fuente, E., & Rodríguez-Esnard, T. 2017, Rev. Mex. Astron. Astrofis., 53, 525